Multivalent Targeting of Blood-Brain Barrier LRP1 for Neurovascular Recovery Therapy for Alzheimer's Disease

Junyang Chen,[1,2,3,4,#] Pan Xiang,[1,2,#,] Aroa Duro-Castano,[4,10] Huawei Cai,[1] Bin Guo,[5] Xiqin Liu [1] Yifan Yu,[1] Su Lui,[1] Kui Luo,[1] Bowen Ke,[1] Lorena Ruiz Perez,[1,3,4,6] Xiawei Wei,[7*] Qiyong Gong,[1,5,8*] Xiaohe Tian[1,2,5,7 *], Giuseppe Battaglia[1,3,4,9*]

[1]Functional and Molecular Imaging Key Laboratory of Sichuan Province, Huaxi MR Research Centre (HMRRC), Department of Radiology, West China Hospital of Sichuan University, Chengdu, 610000, China. [2]Huaxi Xiamen Institute of Medical Research, West China Xiamen Hospital of Sichuan University, Xiamen, Fujian 361021, China. [3]Institute for Bioengineering of Catalunya (IBEC), The Barcelona Institute of Science and Technology, Barcelona (Spain). [4]Department of Chemistry, University College London (UCL), London, UK. [5]The Xiamen Key Laboratory of Psychoradiology and Neuromodulation, Xiamen, China, 361000. [6]Department of Applied Physics, University of Barcelona, Barcelona, Spain. [7]Laboratory of Aging Research and Cancer Drug Target, State Key Laboratory of Biotherapy and Cancer Center and National Clinical Research Center for Geriatrics , West China Hospital, Sichuan University, Chengdu 610041, China. [8]Research Unit of Psychoradiology, Chinese Academy of Medical Sciences, Chengdu, Sichuan, China. [9]Catalan Institution for Research and Advanced Studies (ICREA), Barcelona, Spain.
[10]New address: Curapath, Av. Benjamín Franklin, 19, 46980 Paterna, Valencia
 # These authors contributed equally to this work.

Abstract

We have developed a new method for treating Alzheimer's disease (AD) by targeting the LRP1 receptor at the blood-brain barrier (BBB) using a nanoscopic multivalent scaffold decorated with LRP1 targeting peptides. Our experiments on AD model mice have demonstrated that this treatment significantly reduces amyloid-β (Aβ) deposits and improves cognitive function. This study introduces a new approach to drug design that combines multivalent targeting with controlling membrane trafficking using the same tools for nanocarrier design, creating a novel therapeutic intervention. In doing so, we emphasize the crucial role that the BBB plays in AD pathogenesis, highlighting the vital importance of LRP1-mediated Aβ clearance.

Introduction

Dementia is a term used to describe a decline in cognitive function, which includes memory, thinking, and communication skills, that hinders a person's ability to perform daily activities. Globally, it is the 7th leading cause of death, affecting 45 million people, and is expected to increase dramatically. Alzheimer's disease (AD) accounts for almost 70% of dementia cases among various types. AD pathophysiology is characterized by an accumulation of small peptides, Amyloid-β (Aβ), into fibrils and plaques, followed by hyperphosphorylation, misfolding, and aggregation into neurofibrillary tangles of another protein, tau. Both abnormal

accumulations induce strong inflammatory responses that prompt synaptic dysfunction and neuronal injury, causing considerable brain damage and impairing cognitive processes (1,2). Alongside these, the brain vasculature network, or blood-brain barrier (BBB), plays a critical role during AD progression and possibly initiation. The BBB is made of aligned endothelial cells supported by pericytes and astrocytes, forming the densest vascular network in our body, ensuring about one capillary per neuron. The BBB poses a significant challenge in pharmacology, impeding the penetration of numerous drugs and complicating treatment discovery for neurological disorders (3). Its pivotal role in safeguarding cerebral homeostasis is underscored by its involvement in AD pathogenesis, where abnormalities in the BBB's molecular and cellular functions have been demonstrated (4-6). Most AD patients are often affected by several vascular perturbations (7) traditionally attributed to Aβ accumulations (8). Recent studies have also emphasized the impact on BBB integrity of the hyperphosphorylated tau (9-11).

Clinical research further revealed discernible cerebral capillary damage and compromised BBB integrity independent of Aβ and tau biomarkers (12). This underscores the critical role of the BBB in maintaining brain homeostasis, with its dysfunction involved in the pathogenesis of dementia and AD. Among the various mechanisms the BBB controls, regulating Aβ and tau clearance via the low-density lipoprotein receptor-related protein 1 (LRP1) is particularly crucial (13). Our recent investigations have elucidated the modulatory role of LRP1 in the BBB transport of synthetic nanoparticles and Aβ structures, demonstrating its dependence on cargo avidity (14, 15). Differential pathways of cargo internalization, namely conventional endocytosis into lysosomes for high avidity cargo and transcytosis via tubular vesicles stabilized by PACSIN2 (also named as Syndapin-2) for mid-avidity cargo, have been shown to exert distinct influences on LRP1 expression, leading to its dynamic regulation. Misfolded proteins internalized within the endothelial cells of the BBB can perturb cellular function, leading to stress responses and activation of inflammatory pathways. This disruption can further escalate due to the down-regulation of LRP1 expression in brain endothelial cells, exacerbating the accumulation of misfolded proteins, Aβ brain deposition, and the propagation of tau "seeds," culminating in a reinforcing loop of inflammation (16, 17).

While a recently FDA-approved antibody-based Aβ clearance drug has exhibited cognitive improvements in early to mid-stage AD patients, its utilization is marred by contentious side effects such as brain bleeding and swelling (18-20). In pursuit of a more refined therapeutic approach, our study explores the untapped potential of the LRP1 receptor on AD's BBB. Leveraging a surface-functionalized multivalent scaffold, specifically, Angiopep2 functionalized $P[(OEG)_{10}MA]_{20}$-$PDPA_{120}$ polymersomes (A_{39}-POs) with a defined ligand number. We have already demonstrated we achieve 'super-selective' targeting exclusively at BBB sites expressing LRP1 receptors at specific concentrations (21). This innovative strategy enables precise targeting of AD BBB cells with down-regulated LRP1, inducing robust transport of cerebral Aβ from the brain to the bloodstream. Intravenous administration of A_{39}-POs in our study resulted in a substantial 40% reduction in intracranial insoluble Aβ deposition within a brief therapeutic time window of 2 hours. These findings instill hope for a promising and effective treatment paradigm for AD.

Results and discussion

We employed the Enzyme-Linked Immunosorbent Assay (ELISA) and imaging methods (**Fig. S1**) to conduct a comparative analysis of the whole brain and its vasculature and parenchyma Aβ levels in AD model mice against wild-type controls over a lifespan from 3 to 12 months. We also used ELISA to measure key proteins involved in receptor-mediated transcytosis and endocytosis,

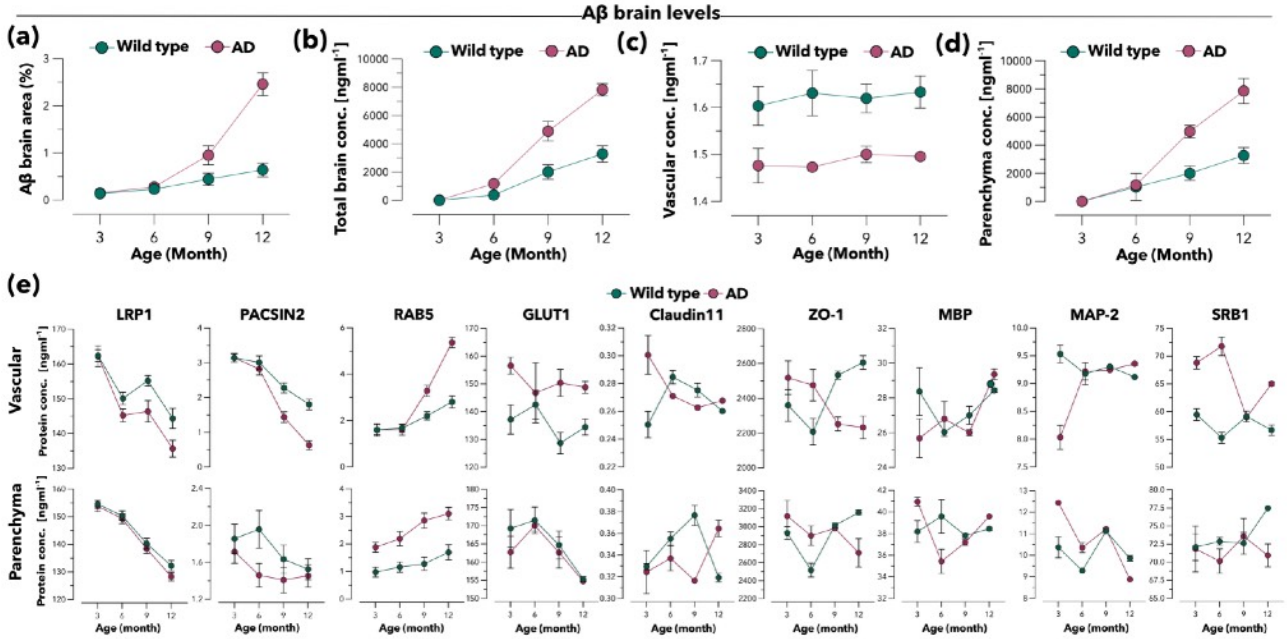

Fig. 1. Comparative analysis of Aβ accumulation and protein expression profiles in AD and wild-type mice. Quantitative representation of Aβ-positive areas (**a**) in brain coronal sections, identified through immune histochemistry (IHC), in both AD model and wild-type mice. Quantitative measurement of Aβ concentrations via ELISA in both AD and wild type mice of the whole-brain (**b**), its vasculature (**c**) and parenchyma (**d**). ELISA quantification of both brain vasculature and parenchyma (**e**) in AD and wild type mice of key proteins involved in trafficking (LRP1, PACSIN2, RAB5), metabolism (GLUT1), tight junction proteins (ZO-1, CLDN11), and other stress-related proteins (MBP, MAP-2, SRB1). For all analyzes (n = 3)

tight junction proteins, neurons, and other associated proteins. We discerned the temporal changes of these proteins from a macroscopic whole brain and BBB. **Fig. 1a** and **Fig. 1b** display the aggregate Aβ levels in the brain, showing a marked rise in Aβ in the AD models with age, a trend particularly pronounced between 6 to 12 months. A measurable disparity in BBB Aβ levels between the AD model mice and the wild-type controls is evident in **Fig. 1c**, revealing significantly higher Aβ in the brain's vasculature of wild-type mice, with notable differences emerging at all lifespan stages, emphasizing the pathological hallmarks of AD with its deficient BBB transport capacity.

Conversely, **Fig. 1d** delineates the parenchymal Aβ concentration, indicating a significant surge in the AD models, especially between 9 to 12 months. The following ELISA assessment shows the changes in various protein levels in the brain's vascular and parenchymal regions in AD model mice and wild-type controls over the same period. We focused on LRP1, PACSIN2, RAB5, GLUT1, Claudin 11, ZO-1, MBP, MAP-2, and SRB1, which are essential for processes like transcytotic transport, lipid transport, glucose metabolism, and the maintenance of cellular structure and integrity. Notable variations were observed throughout the months, with proteins like MBP and MAP-2, essential for neural integrity, displaying divergent trends potentially indicative of neurodegenerative alterations characteristic of AD (**Fig. 1e**). We also observed that the transcytosis-related proteins LRP1 and PACSIN2 (14,15) showed marked reductions on vascular endothelial cells as AD advanced. Meanwhile, RAB5, integral to endocytosis, and GLUT1, essential for glucose transport across the BBB, demonstrated noticeable increments correlating with AD progression. Fluorescent images showed the same trend (**Fig. S2**).

Following the clue upon analyzing the brain vascular protein variation, we then use confocal microscopy images that showcase the spatial localization of LRP1 and Aβ at the BBB endothelium (CD31) and pericytes (CD146) in 3-month-old and 12-month-old AD brain samples. **Fig. 2a** (3-month-old), Aβ (red) is highly co-localized with LRP1 (white) on the surface of blood vessel cells of the BBB (green), suggesting active involvement of LRP1 in Aβ transport and clearance at a younger age, with less Aβ accumulation around the vessels.

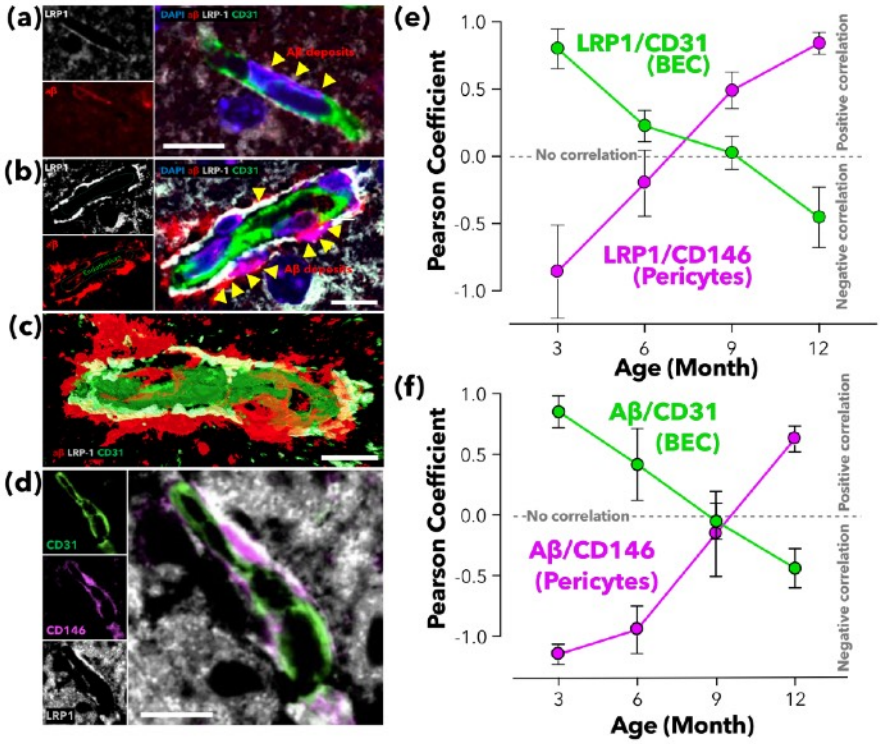

Fig. 2. Confocal microscopy and co-localization analysis of brain endothelial cells, pericytes, and Aβ in AD mice of different ages. LRP1 (grey), Aβ (red), and BBB endothelium (CD31, green) in 3-month-old (**a**) and in 12-month-old (**b**) AD mice brain samples. 3D rendering (**c**) of the 12-month-old AD brain section highlighting the spatial relationship between the different markers. In later AD stages, increased Aβ accumulation near the BBB and reduced co-localization of CD31 with LRP1 are observed. CD31, CD146, and LRP1 in a 12-month-old AD brain sample (**d**). Scale bar = 10 μm. Pearson correlation coefficients over different ages for LRP1 (**e**) and Aβ (**f**) with endothelial cells (CD31) and pericytes (CD146), showing changing interaction patterns with ageing.

Fig. 2b shows 12-month-old brains, and its corresponding 3D image (**Fig. 2c**) indicates a noticeable increase in Aβ deposition on the basal side of the BBB vessels. The co-localization of LRP1 with Aβ appears to decrease, potentially signifying impaired LRP1-mediated clearance of Aβ as AD progresses. At later stages of AD, the increased Aβ accumulation and reduced association with LRP1 may affect BBB function and promote disease pathology. Interestingly, further image (**Fig. 2d**) suggests LRP1 appears predominantly deposited around the pericytes on the exterior side of the BBB blood vessels. We further analyze representative brain sections from 3-12 months, labeling LRP1, Aβ, and pericytes and endothelium markers CD146 and CD31, respectively. We performed a co-localization analysis and calculated the Pearson correlation coefficient between LRP1 and CD31 and between LRP1 and CD146. In **Fig. 2e**, the results show a trend where the association between LRP1 and endothelial cells weakens over time (green line), while its correlation with pericytes appears to strengthen (purple line). Similarly, the same analysis with Aβ shows a Pearson correlation coefficient over time with both endothelial cells (green line) and pericytes (purple line) an inverse association (**Fig. 2f**). Combining the above ELISA and confocal evaluation, the shift in LRP1 from BBB vascular endothelium to pericytes with aging underscores a potentially pivotal role in the pathophysiology of AD. This progression suggests a decrease in LRP1-mediated Aβ clearance at the BBB endothelial level, with a concomitant increase

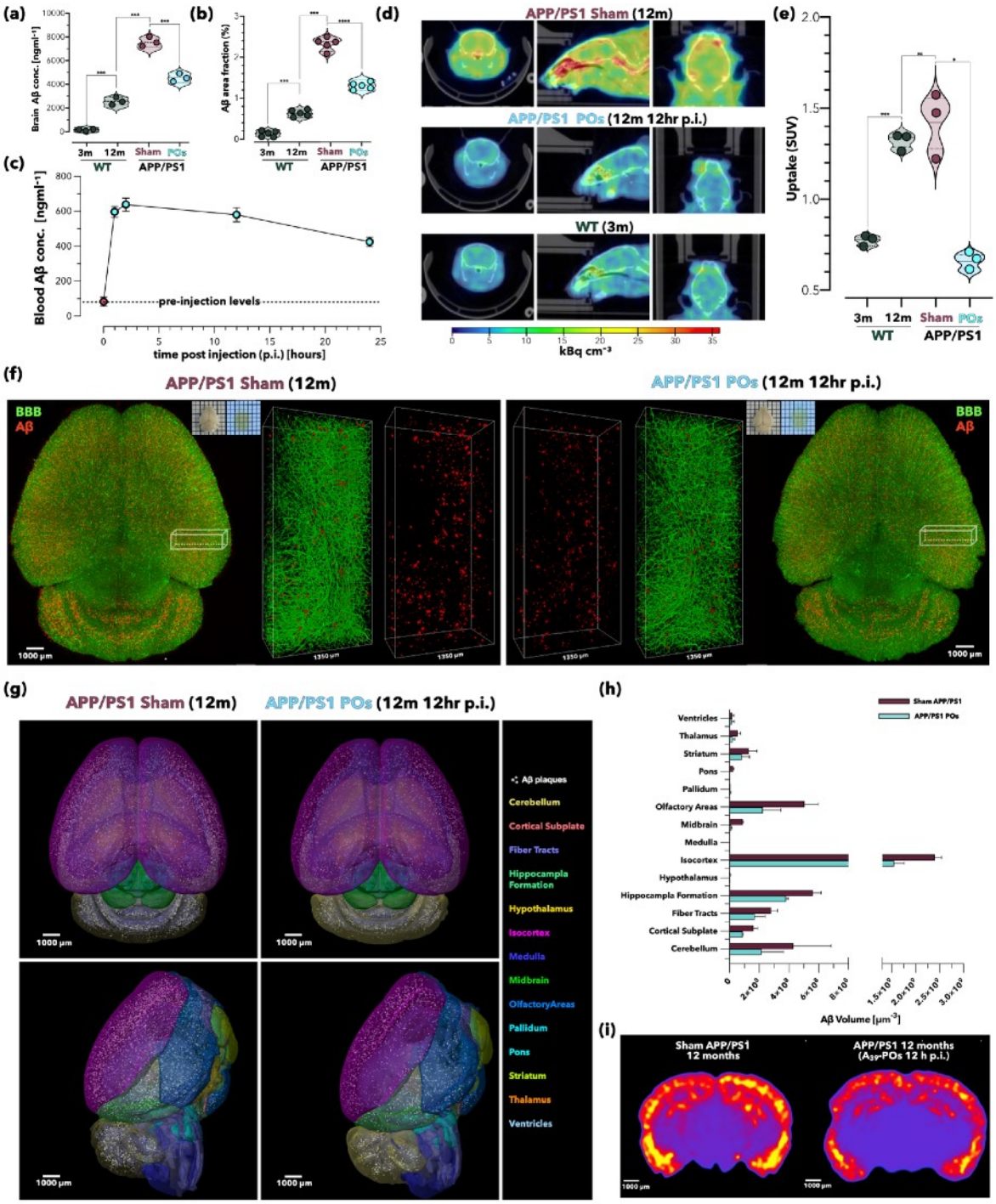

Fig. 3. A_{39}-POs reduce Aβ levels in the brains of AD mice. ELISA measurement of whole-brain Aβ levels 2 hr post A_{39}-POs administration (**a**) revealed significant reductions, from ~7500 ng/ml to ~4500 ng/ml. Quantification of Aβ positive area fraction on IHC stained coronal brain sections (**b**). Temporal Aβ concentration profile in blood (**c**) post A_{39}-POs injection, sampled at 0, 1 , 2, 12 , and 24 hr. PET-CT whole body imaging (**d**) of wild type (3 and 12 months old) and APP/PS1 (12-month-old pre- and 12 h post A_{39}-POs injection) mice following [^{18}F]AV-45 (2.8-3.2 MBq) administration 1 h prior to scanning. Standardized uptake value (SUV) of [^{18}F]-AV45 (**e**) indicating a significant post treatment Aβ level decrease in the brain. 3D rendering from light sheet fluorescence imaging (**f**) of brain after tissue clearing shows reduced Aβ signals (in red) in A_{39}-POs treated mice at 12 h. Brain region mapping (**g**) with noted reduction in Aβ plaques in the isocortex. Brain segmentation into 14 regions revealing predominant Aβ distribution in the isocortex, with a total volumetric reduction of 41% post A_{39}-POs treatment (**h**). Thermal map representation of Aβ fluorescence intensity across a single coronal brain layer (**i**). Tissue clearing experiments were conducted at least twice per group. Statistical significance was determined using One-way Analyzes of Variance (ANOVA), *p<0.05, **p<0.01, ***p<0.001, ****p<0.0001, n = 3.

associated with pericytes, which may impact AD progression.

Our previous studies (14, 21) found that the peptide Angiopep2 can target LRP1. We also discovered that the efficiency of crossing the BBB is higher when the ligand is present on a multivalent scaffold. Our research has shown that the transportation of LRP1 across the BBB occurs through transcytosis (14). This process involves collective endocytosis and exocytosis and is regulated by a BAR domain protein called PACSIN2. Our observation suggests that cargo with an intermediate number of ligands works best with this transportation mechanism. This includes synthetic cargos like A_{39}-PO polymersomes (14) and natural cargos like Aβ assemblies (15). Both multivalent units trigger PACSIN2-mediated transcytosis. In both synthetic cargo and Aβ assemblies, PACSIN2-mediated transcytosis coincided with a temporary up-regulation of the LRP1 receptor (14, 15). Therefore, we hypothesize that using LRP1 multivalent targeted nanoparticles may restore the function of LRP1 in transporting Aβ out from the brain and

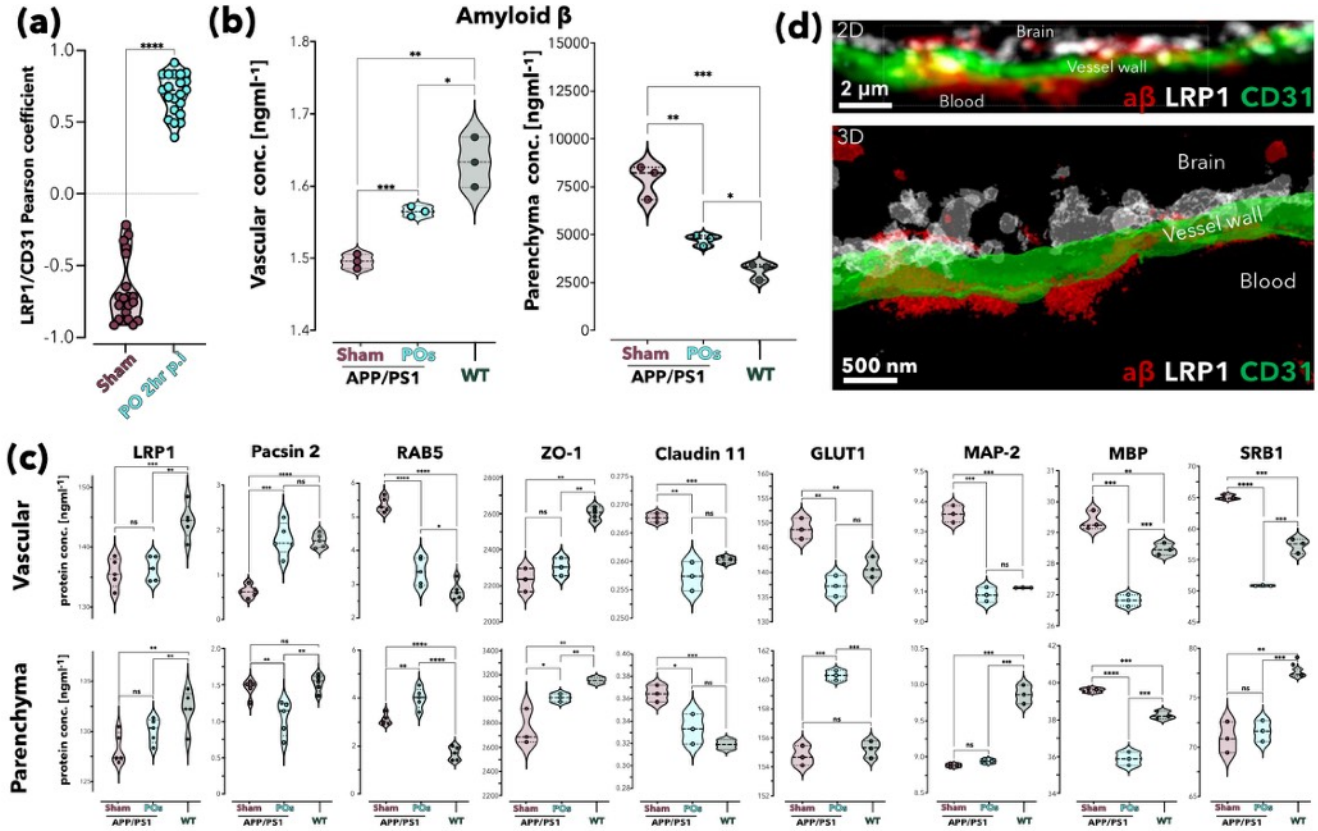

Fig. 4. A_{39}-POs treatment restores healthy BBB phenotype. Pearson correlation coefficients for the colocalization of LRP1 and BBB endothelial cells (CD31) pre- and post A_{39}-POs administration (**a**). Analysis performed on images derived from three independent experiments, with 6-7 vessels studied per trial. Quantification of Aβ content in cerebrovascular endothelial cells and brain parenchyma (**b**) (n = 3, statistical analyzis performed using unpaired t-tests, **** $p<0.0001$). ELISA measurements (**c**) of vascular and parenchymal proteins in 12-month-old WT, Sham APP/PS1, and APP/PS1 post A_{39}-POs treatment mice, encompassing LRP1, PACSIN2, RAB5, GLUT1, Claudin 11, ZO-1, MBP, MAP-2, and SRB1. STED microscopy (**d**) of LRP1 (white) on the vessel wall (green), indicative of active transcytosis. Post-treatment, Aβ deposits around the BBB (red) are cleared with notable Aβ signal presence within the vascular lumen. For (b) and (c), statistical significance determined using one-way ANOVA, *$p<0.05$, **$p<0.01$, ***$p<0.001$, ****$p<0.0001$, $n \geq 3$.

potentially have the effect of clearing Aβ deposits in the AD model. We prepared and characterized Angiopep2-P[(OEG)$_{10}$MA]$_{20}$-PDPA$_{120}$ polymersomes bearing 39 ligands per particle from now on, referred to as A$_{39}$-POs (**Fig. S3**). APP/PS1 transgenic AD mouse was intravenously (i.v.) injected with A$_{39}$-POs (10 g/L, 200 μL), and ELISA analyzed the whole brain. The Aβ contents showed a 40% reduction after a short administration period (**Fig. 3a**), from 7500 ng/mL to 4500 ng/mL. A parallel immune histochemistry (IHC) analysis confirmed that the

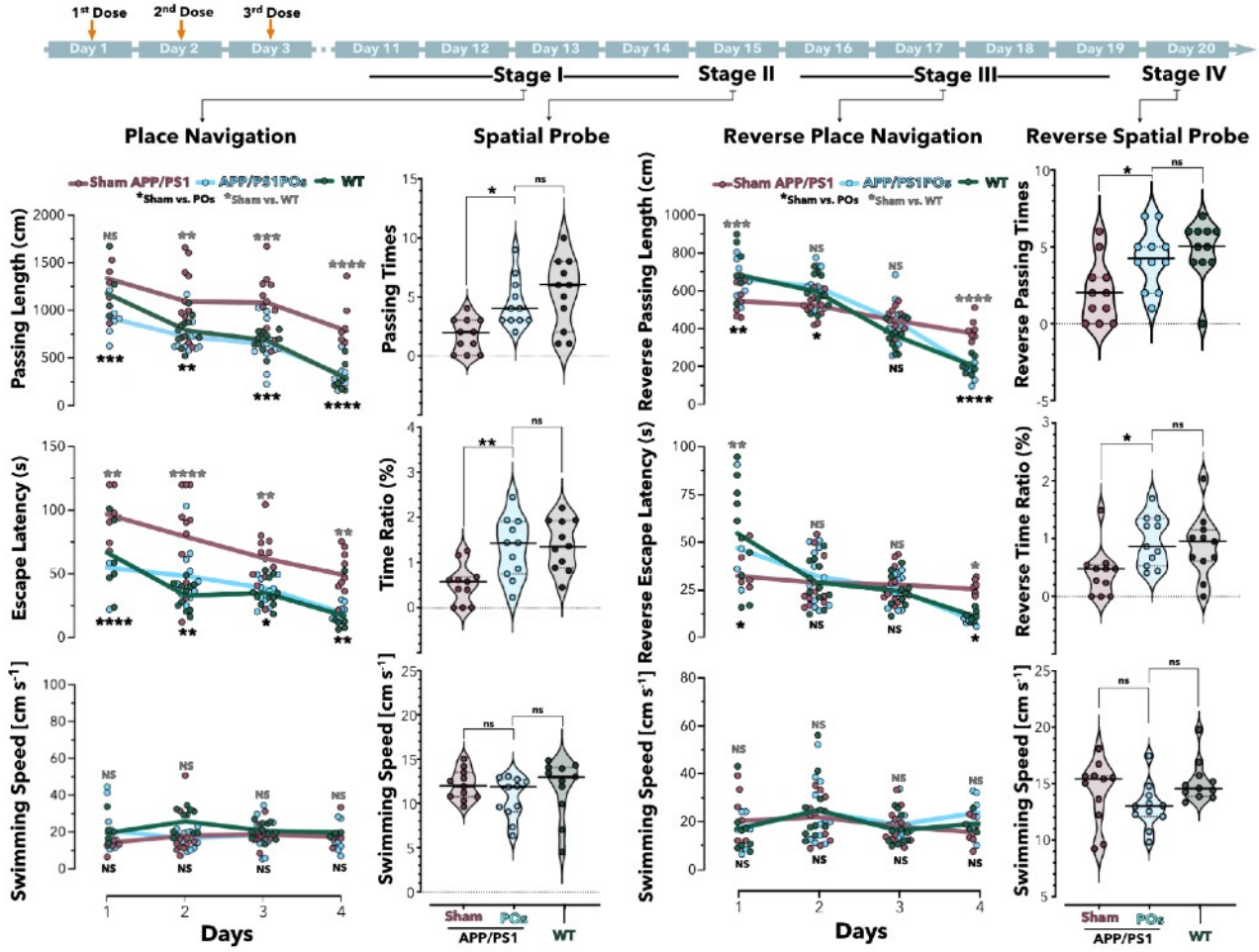

Fig. 5. Behavioural tests demonstrated that A$_{39}$-POs treatment improved cognitive performance in AD model mice. Mice were injected with saline (Sham APP/PS1 group and WT group, 200 μL) or A$_{39}$-POs (APP/PS1 POs group, 10 g/L 200 μL) once daily for the first three mornings. Recovery was observed from days 4 to 10 under original rearing conditions. (Stage I) Place navigation test occurred on days 11-14, showing a gradual decrease in passing length and escape latency for finding the escape platform across all groups, with the APP/PS1 POs group matching the WT level and significantly outperforming the Sham APP/PS1 group. (Stage II) On day 15, during the spatial probe, both the APP/PS1 POs and WT groups demonstrated more passing times and a higher percentage of time spent at the escape platform's original location. (Stage III) The reverse place navigation trial from days 16-19, with the platform moved to the opposite side, saw the APP/PS1 POs and WT groups initially taking longer, indicating stronger spatial memory from stage I and stage II. However, their reverse passing length and escape latency decreased rapidly over time and were significantly lower than those of the Sham APP/PS1 mice. (Stage IV) On day 20, in the reverse spatial probe test without the platform, A$_{39}$-POs treated mice still outperformed the Sham APP/PS1 group. Place navigation trials (Stages I and III) were analyzed using two-way ANOVA, while spatial probe trials (Stages II and IV) comparisons used one-way ANOVA. Significance levels are denoted as *p<0.05, **p<0.01, ***p<0.001, ****p<0.0001, with n = 11.

Aβ area fraction also decreased (**Fig. 3b** and **Fig. S5**). The brain reduction is mirrored by an increase in blood Aβ concentration, proving that the Aβ is shuttling from the brain to blood (**Fig. 3c**). Furthermore, we employed Positron Emission Tomography-Computed Tomography (PET-CT) to assess the clearance of Aβ in the brains of live animals. We utilized (E)-4-(2-(6-(2-(2-(2-^{18}F-fluoroethoxy)ethoxy)ethoxy)pyridin-3-yl)vinyl)-N-methyl benzamine ([^{18}F]AV-45), which has been previously demonstrated to strongly correlate with the presence and density of Aβ (22). We thus imaged the brains of young (3-month-old) wild-type mice as controls. The PET-CT scans revealed that the brain of a 12-month-old APP/PS1 mouse exhibits an intense Aβ signal. In contrast, this signal sharply decreased in the treated APP/PS1 mice (**Fig. 3d**). Following the administration of A_{39}-POs, the Standardized Uptake Value (SUV) associated with Aβ reduction was 40.6% and 46.25% (overnight) (**Fig. 3e**). We finally performed tissue clearing on brains of Sham AD 12-month-old and A_{39}-POs treated 12-month-old AD mice. The Aβ (red) and BBB (green) of these brains were labeled, respectively (**Fig. 3e**). Brains of mice treated by A_{39}-POs had less Aβ signal relative to the Sham AD brain. 3D brain images were nested into the Amira software companion brain partitioning model and paired (**Fig. 3g**). Aβ volume in 14 brain regions of the mouse brain was measured separately (**Fig. 3h**). A total of 41% reduction in mice brain Aβ volume after treatment with A_{39}-POs. Lastly, coronal Aβ distribution is shown as a heat map in **Fig. 3i**.

The above outcomes motivated us to re-study the BBB vasculature phenotype after A_{39}-POs treatment. We first observed a reserve of the co-localization of LRP1 with CD31 in the mouse brain, as shown in **Fig 4a** and **Fig. S7**; the overlap of LRP1 and BBB endothelial cells (CD31) returned to the state of wild-type. We thus analyzed the Aβ content in brain vascular endothelial cells and parenchyma and found a significant increase in its content in BBB and a notable decrease in parenchyma (**Fig. 4b**). The ELISA assessments again are performed to indicate proteins in both vascular and parenchymal after A_{39}-POs treatment in 12-month-old AD mice (**Fig. 4c**). As discussed previously, the analysis focuses on the concentrations of various proteins such as LRP1, PACSIN2, RAB5, GLUT1, Claudin 11, ZO-1, MBP, MAP-2, and SRB1. The nanomedicine drug cleared Aβ and caused a rapid change in the BBB phenotype by up-regulating PACSIN2 and down-regulating RAB5. This finding is consistent with our confocal data, which shows that LRP1 relocates to blood vessels. The morphology of LRP1 (white), observed under a stimulated emission depletion (STED) microscope, showed clustered distribution upon the vessel wall (green), suggesting robust ongoing transcytosis. We also observed that the Aβ deposition (red) around the BBB disappeared, and confocal images displayed a large amount of Aβ signal in the vascular lumen (**Fig. 4d**).

Finally, we showed the effect of A_{39}-POs administration on animal cognition using enhanced spatial learning and memory. As indicated in **Fig. 5**, the phase one data showed that compared to the Sham APP/PS1 group, the APP/PS1 POs group could find the escape platform via a shorter path, indicating that the mice have a similar search strategy to the wild types. Their spatial learning and memory abilities are superior to those of the Sham APP/PS1 group. The escape latency (time taken to find the escape platform) of the APP/PS1 POs group was also shorter. As the experiment days increased, the time animals took to find the platform gradually decreased, suggesting that they made progress in learning and remembering the platform's location. A shorter escape latency indicates the animals' better spatial learning and memory abilities. Although the relationship between swimming speed and spatial learning and memory abilities is weak, analyzing swimming speed can rule out the impact of the animals' motor abilities or fear during the experiments. For all parts, there was no statistical difference in the swimming speeds of the three groups of mice.

When the experiment entered the second phase, and the escape platform was removed, the

APP/PS1 POs group crossed the platform more times and spent a significantly larger percentage of time at the platform's original location than the Sham APP/PS1 group, reflecting stronger long-term memory of the platform's location. The nearly indistinguishable swimming speeds during this phase suggest a minimal impact on motor abilities or fear of the animals. When the escape platform was placed on the opposite side of its original location. Initially, longer search times reflected a long-term memory of the original platform's location. Still, as the number of training sessions increased, the group with stronger learning abilities (APP/PS1 POs group) showed a higher rate of reduction in path length and escape latency. In the last two days of this phase, animals treated with A_{39}-POs showed shorter escape paths and shorter escape latencies. The swimming speeds of the animals were almost indistinguishable during this phase. When the escape platform was removed, the APP/PS1 POs group stayed longer at the escape location. It crossed this location more times, reflecting the stronger memory abilities of the animals treated with A_{39}-POs, with nearly no difference in swimming speeds during this phase. Overall, the behavioral experiments indicate that animals treated with A_{39}-POs showed improved navigation and learning capabilities and exhibited cognitive enhancements attributed to the rapid clearance of Aβ following A_{39}-PO treatment.

Conclusion

Our study represents a significant innovation in AD therapeutics by employing a multivalent targeting approach using Angiopep2 functionalized polymersomes to modulate LRP1 receptors. This strategy has successfully achieved rapid clearance of Aβ, leading to an immediate alteration in the BBB phenotype and a reversal in AD pathology. The treatment has diminished Aβ deposits and brought about a swift change in the vascular and parenchymal protein profiles, indicative of a restored BBB function. The observed cognitive improvements in AD mice underline the effectiveness of our approach, suggesting a promising new direction for AD treatment that combines targeted Aβ clearance with BBB phenotype modulation.

Acknowledgments

This study was supported by the National Key R&D Program of China (2022YFC2009900), the Alzheimer's Association New to the Field award, ERC Consolidator grant H2020-ERC-2018-CoG (769798 CheSSTag), Plan de Recuperacion Nacional Biotech for Health Project (ADNano), Activitat científica dels grups de recerca de Catalunya (SGR-Cat 2021), and Spanish Research Agency Proyectos I+D+I PID2020-119914RB-I00.

References

1. H. Hampel *et al.*, The Amyloid-beta Pathway in Alzheimer's Disease. *Mol Psychiatry* **26**, 5481-5503 (2021).
2. E. Karran, B. De Strooper, The amyloid hypothesis in Alzheimer disease: new insights from new therapeutics. *Nature Reviews Drug Discovery* **21**, 306-318 (2022).
3. C. Kurz, L. Walker, B. S. Rauchmann, R. Perneczky, Dysfunction of the blood-brain barrier in Alzheimer's disease: Evidence from human studies. *Neuropathol Appl Neurobiol* **48**, e12782 (2022).

4. Z. Arvanitakis, A. W. Capuano, S. E. Leurgans, D. A. Bennett, J. A. Schneider, Relation of cerebral vessel disease to Alzheimer's disease dementia and cognitive function in elderly people: a cross-sectional study. *Lancet Neurol* **15**, 934-943 (2016).
5. K. Kisler, A. R. Nelson, A. Montagne, B. V. Zlokovic, Cerebral blood flow regulation and neurovascular dysfunction in Alzheimer disease. *Nat Rev Neurosci* **18**, 419-434 (2017).
6. Y. Iturria-Medina *et al.*, Early role of vascular dysregulation on late-onset Alzheimer's disease based on multifactorial data-driven analysis. *Nat Commun* **7**, 11934 (2016).
7. J. M. Wardlaw *et al.*, Neuroimaging standards for research into small vessel disease and its contribution to ageing and neurodegeneration. *Lancet Neurol* **12**, 822-838 (2013).
8. K. A. Jellinger, Alzheimer disease and cerebrovascular pathology: an update. *J Neural Transm (Vienna)* **109**, 813-836 (2002).
9. R. E. Bennett *et al.*, Tau induces blood vessel abnormalities and angiogenesis-related gene expression in P301L transgenic mice and human Alzheimer's disease. *Proc Natl Acad Sci U S A* **115**, E1289-E1298 (2018).
10. Y. Moon *et al.*, Blood-brain barrier breakdown is linked to tau pathology and neuronal injury in a differential manner according to amyloid deposition. *J Cereb Blood Flow Metab* **43**, 1813-1825 (2023).
11. R. A. Fisher, J. S. Miners, S. Love, Pathological changes within the cerebral vasculature in Alzheimer's disease: New perspectives. *Brain Pathol* **32**, e13061 (2022).
12. D. A. Nation *et al.*, Blood-brain barrier breakdown is an early biomarker of human cognitive dysfunction. *Nat Med* **25**, 270-276 (2019).
13. M. D. Sweeney, K. Kisler, A. Montagne, A. W. Toga, B. V. Zlokovic, The role of brain vasculature in neurodegenerative disorders. *Nat Neurosci* **21**, 1318-1331 (2018).
14. X. Tian *et al.*, On the shuttling across the blood-brain barrier via tubule formation: Mechanism and cargo avidity bias. *Sci Adv* **6**, (2020).
15. M. L. D *et al.*, Syndapin-2 mediated transcytosis of amyloid-beta across the blood-brain barrier. *Brain Commun* **4**, fcac039 (2022).
16. Q. Liu *et al.*, Amyloid precursor protein regulates brain apolipoprotein E and cholesterol metabolism through lipoprotein receptor LRP1. *Neuron* **56**, 66-78 (2007).
17. J. M. Cooper *et al.*, Regulation of tau internalization, degradation, and seeding by LRP1 reveals multiple pathways for tau catabolism. *J Biol Chem* **296**, 100715 (2021).
18. C. H. van Dyck *et al.*, Lecanemab in Early Alzheimer's Disease. *N Engl J Med* **388**, 9-21 (2023).
19. N. J. Reish *et al.*, Multiple Cerebral Hemorrhages in a Patient Receiving Lecanemab and Treated with t-PA for Stroke. *N Engl J Med* **388**, 478-479 (2023).
20. S. Reardon, Alzheimers drug donanemab what promising trial means for treatments. **617**, (2023).
21. X. H. Tian, S. Angioletti-Uberti, G. Battaglia, On the design of precision nanomedicines. *Science Advances* **6**, (2020).
22. C. M. Clark *et al.*, Use of Florbetapir-PET for Imaging β-Amyloid Pathology. *Jama-Journal of the American Medical Association* **305**, 275-283 (2011).

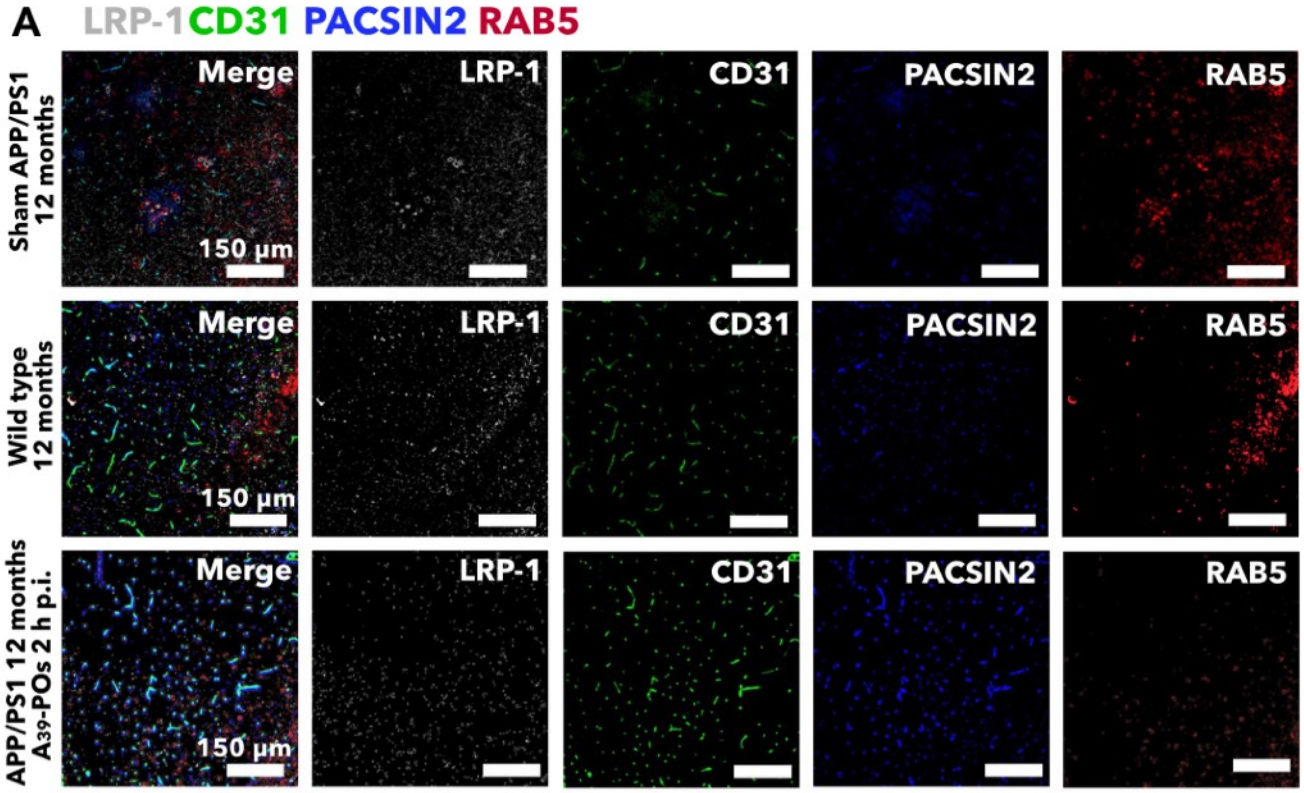
A
LRP-1 CD31 PACSIN2 RAB5
Sham APP/PS1 12 months
Wild type 12 months
APP/PS1 12 months A39-POs 2 h p.i.
Merge
LRP-1
CD31
PACSIN2
RAB5
150 µm

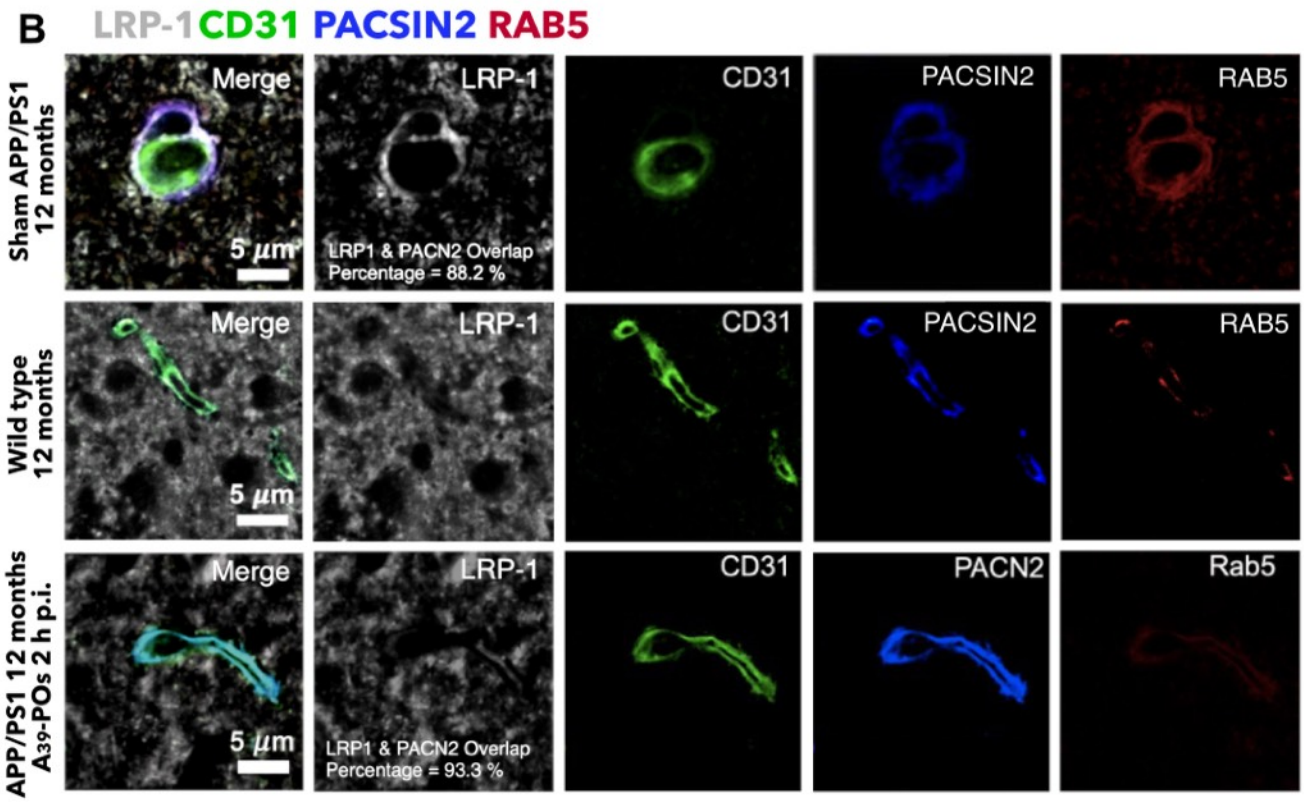
B
LRP-1 CD31 PACSIN2 RAB5
Sham APP/PS1 12 months
Wild type 12 months
APP/PS1 12 months A39-POs 2 h p.i.
Merge
LRP-1
CD31
PACSIN2
PACN2
RAB5
Rab5
5 µm
LRP1 & PACN2 Overlap Percentage = 88.2 %
LRP1 & PACN2 Overlap Percentage = 93.3 %

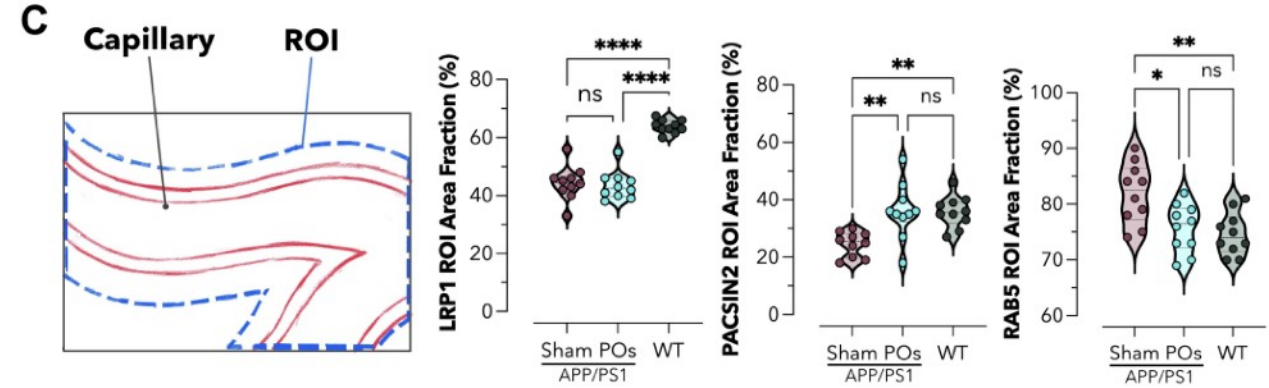
C
Capillary
ROI
LRP1 ROI Area Fraction (%)
PACSIN2 ROI Area Fraction (%)
RAB5 ROI Area Fraction (%)
Sham POs
WT
APP/PS1
ns
****
**
*

Supporting information Table of contents

Supporting information……3
1. Materials and methods……3
A_{39}-POs Polymersome Preparation and Characterisation……3
Animal Experiments……3
Immunohistochemistry (IHC)……5
Aβ Extraction……5
Vessel Extraction……5
Enzyme-Linked Immunosorbent Assay (ELISA)……6
Confocal Imaging……7
Tyramide Signal Amplification (TSA) Stain……7
Positron Emission Tomography-Computed Tomography (PET-CT) Imaging……8
Hematoxylin-Eosin Staining (H&E) Stain……9
Tissue Clearing and Staining……9
High Performance Liquid Chromatography (HPLC)……10
Morris Water Maze (MWM) Experiment ……11
2. Extended figures……13
Fig. S1. IHC images of Aβ in the brains sections of age-matched mice……13
Fig. S2. Fluorescence micrographs colocalisation analysis of age-matched brains……14
Fig. S3. Characterization of A_{39}-POs in terms of size and morphology……15
Fig. S4. The administration of A_{39}-POs markedly increased the concentration of blood Aβ within a brief timeframe……16
Fig. S5. IHC images of Aβ in the brain sections of 12-month-old Sham APP/PS1 and A_{39}-POs treated mice……17
Fig. S6. Brain clearing images of 12-month-old Sham APP/PS1 and A_{39}-POs treated mice……18
Fig. S7. Fluorescence micrographs co-localisation analysis of treated brain……19
Fig. S8. Blood biochemical tests to evaluate the biosafety of A_{39}-POs……21
Fig. S9. H&E staining to evaluate the biosafety of A_{39}-POs……22
Fig. S10. HPLC methodology was employed to ascertain the encapsulation efficiency following the encapsulation of Donepezil within A_{39}-POs……24
Fig. S11. Donepezil@POs can treat AD and produce similar therapeutic effects to A_{39}-POs, which are superior to the same dosage of free donepezil……25
References……27

Supporting information

1. Materials and methods

A_{39}-POs Polymersome Preparation and Characterisation

P[(OEG)$_{10}$MA]$_{20}$-PDPA$_{120}$ and Angiopep2-P[(OEG)$_{10}$MA]$_{20}$-PDPA$_{120}$ copolymers were synthesised via atom transfer radical polymerisation (ATRP) as previously reported (1). A_{39}-POs were formulated utilising the film-rehydration method, whereby P[(OEG)$_{10}$MA]$_{20}$-PDPA$_{120}$ and a 1.88 % molar ratio of Angiopep2-P[(OEG)$_{10}$MA]$_{20}$-PDPA$_{120}$ were dissolved in a methanol and chloroform mixture (v/v, 3:1). The mixture was left to evaporate, allowing the organic solvent to completely dissipate and form a homogeneous polymer film at the bottom of the vessel. PBS solution was added to rehydrate the polymer film (10 g/L) and sonicated for 30 min. The solution was stirred continuously for 7 days at 4°C using a magnetic stirrer at 1000 rpm. The morphology of A_{39}-POs was examined via transmission electron microscopy (JEM-2100Plus, Japan). Diameter distribution was assessed by dynamic light scattering (Malvern Zetasizer Pro, UK).

Animal Experiments

All animal studies were conducted in accordance with the guidelines set forth by the *West China Hospital Animal Care Committee*. Considerable efforts were made to minimise the number of animals utilised in these studies and to

alleviate any pain or discomfort experienced by the animals. In all experiments, animals were accommodated in a room where the temperature was regulated, with consistent alternating cycles of light and darkness. All experiments were carried out using male mice.

Immunohistochemistry (IHC)

Paraffin-embedded sections (5 μm) of mouse brain tissue were deparaffinised with xylene and subjected to gradient alcohol dehydration (30%, 50%, 80%, 100%). Endogenous peroxidase activity was quenched using 3% H_2O_2 (room temperature, 10 min) following antigen retrieval (Biosharp, 22315828). The tissues were blocked with 1% BSA (Aladdin, A104912) at room temperature for 30 min. Aβ targeting primary antibodies were applied overnight at 4°C (Servicebio, GB13414-1, 1:200), followed by washing with PBS. The sections were then incubated with HRP-conjugated secondary antibodies (Abclonal, AS014, 1:150) at ambient temperature for 30 min and subsequently washed with PBS. DAB substrate (Elabscience, E-IR-R101, 1:20) and haematoxylin differentiation solution (Servicebio, G1004) were sequentially applied to the sections for 5 min each. The sections were further treated with haematoxylin solution (Servicebio, G1039) at room temperature for 1 min, followed by a PBS wash. After another PBS wash, sections were counterstained with Dako bluing

buffer (Servicebio, G1040) at room temperature for 1 min. Lastly, the slides were mounted using a quick-drying neutral resin (ZSZSGBBIO, ZLI-9516).

Aβ Extraction:

Following euthanasia via an overdose of isoflurane anaesthesia, cardiac perfusion was conducted with cold PBS. Subsequently, the entire brain tissue was harvested and weighed. The brain tissues underwent comprehensive homogenisation (Servicebio, KZ-5F-3D) employing a TBS solution imbued with phosphatase inhibitor (Servicebio, CR2302054) and protease inhibitor (Servicebio, CR2306008) at 70 Hz, -20°C. The supernatant was segregated subsequent to centrifuging the brain tissue homogenate for 1 h at 100,000g and 4°C utilising an ultra-high-speed centrifuge (Beckman, Optima MAX-XP). The tissue residue was then reprocessed. The residues were resuspended in 70% formic acid (Aopusheng (Tianjin) Chemical, 20210610), centrifuged at 100,000g, 4°C for 1 h, and the resultant supernatant was collected.

Vessel Extraction

Immediately following euthanasia via isoflurane overdose anaesthesia, the heart was perfused with cold PBS, and brain tissues were excised and weighed. The tissues were processed using a vascular parenchyma isolation buffer

comprising 10 mM HEPES (Servicebio, CR2207064), 141 mM NaCl (Aladdin, 111549), 4 mM KCl (Aladdin, P112134), 2.8 mM $CaCl_2$ (Aladdin, C290953), 1 mM $MgSO_4$ (Aladdin, M433513), 1 mM NaH_2PO_4 (Aladdin, S433623), and 10 mM glucose (Servicebio, CR2112094). Fresh brain tissue underwent vascular and parenchymal separation. To 500 μL of brain tissue homogenate, 1 mL of 26% (w/w) dextran (Next Sage, 61212ES60) was added. Following thorough mixing and a resting period of 15 min at 4°C, the mixture was centrifuged (15,800g, 15 min, 4°C). Subsequently, the upper layer represented the parenchymal fraction, and the lower layer corresponded to the vascular fraction, with both fractions being thoroughly rinsed with PBS.

Enzyme-Linked Immunosorbent Assay (ELISA)

Mice were euthanised through an overdose of isoflurane anaesthesia. They were then perfused with cold PBS, and their brain tissues were excised and weighed. The brain tissues underwent comprehensive homogenisation using a tissue lysis solution (Yase, 016c1050) enhanced with a phosphatase inhibitor (Servicebio, CR2302054) and a protease inhibitor (Servicebio, CR2306008) at 70 Hz, -20°C. The tissues were allowed to fully lyse by resting at 4°C for 15 min. The supernatant was collected via centrifugation at 14,000 g, 4°C for 10 min. Protein concentrations for various proteins, including LRP1 (NOVUS,

NBP3-00449), PACSIN2 (Anruike, YX-160103M), RAB5 (abbexa, abx154598), GLUT1 (Anruike, YX-071242M), Claudin11 (Anruike, YX-031229M), ZO1 (Elabscience, E-EL-M1161), MBP (Elabscience, E-EL-M0805), MAP-2 (Anruike, YX-120118M), SRB1 (Anruike, ARK-756321A), and Aβ (invitrogen, KMB3441) were determined using ELISA kits following the manufacturer protocols. Protein concentrations were calculated based on the curve equation (four-parameter fit).

Confocal Imaging

Confocal images were captured using a Leica Stellaris 5 confocal microscope, equipped with Diode 405, Argon, DPSS 561, and HeNe633 lasers. Imaging was conducted at a resolution of 2048×2048 pixels and a scanning speed of ×100. Colocalisation analysis to derive Pearson's correlation coefficient r was performed utilising the colocalisation plug-in on ImageJ.

Tyramide Signal Amplification (TSA) Stain

Mouse brain tissue sections were deparaffinised with xylene and rehydrated through gradient alcohol dehydration. Following antigen retrieval, 3% H_2O_2 was utilised to inactivate endogenous peroxidase in tissues (Biosarp, 22315828) for 10 min. Permeabilisation of sections at room temperature for 10 min was

achieved using 1% Triton X-100 (Biofroxx, 1139ML100). The sections were rinsed with PBS and incubated with the primary antibody solution for 1 h at room temperature. After washing with PBS, the samples were incubated with the HRP-conjugated secondary antibody for 10 min. Subsequent to a PBS rinse, the TSA fluorescent solution (Absin, abs50031) was applied and incubated at room temperature for 10 min. Antigen repair was subsequently conducted. The aforementioned steps were reiterated with distinct primary antibodies, including LRP1 (abclonal, A1439, 1:100), Aβ (servicebio, GB13414-1, 1:200), CD31 (cellsignaling, 77699, 1:300), RAB5 (thermofisher, PA5-88260, 1:200) and CD146 (abcam, ab75769, 1:300), and various wavelengths of TSA, encompassing TSA520, TSA570, TSA620, and TSA700 dyes until multimeric fluorescent staining was achieved. Upon completion of the final staining cycle, nuclei were stained with DAPI (Solarbio, C0065) for 5 min, then sealed with antifade sealing agent (Solarbio, S2100).

Positron Emission Tomography-Computed Tomography (PET-CT) Imaging

Normal saline (200 μL) were intravenously administered to wild type mice (3 and 12 months old) and sham APP/PS1 mice (12-month-old), and 200 μL of A_{39}-POs (10 g/L) were intravenously injected into APP/PS1 mice (12-month-old). Twelve hours subsequent, all mice received an intravenous injection of the

commercial Aβ radiocontrast agent [^{18}F]AV-45 (2.8-3.2 MBq). One hour subsequent, images of the mice's intracranial centroids were acquired using a Micro-PET-CT imager (France Inviscan).

Hematoxylin-Eosin Staining (H&E) Stain

Mouse tissue sections (5 μm) were dewaxed and rehydrated. The sections were stained with haematoxylin solution for 5 min, followed by incubation with differentiation solution (Servicebio, G1039) for 10 - 15 s. Subsequently, the sections were treated with Dako bluing solution (Servicebio, G1040) for 30 s and washed with PBS. After air-drying, the sections were stained with eosin staining solution for 30 s, followed by washing with ethanol. The slides underwent dehydration through a gradient of ethanol (30%, 50%, 80%, 100%) and xylene. Finally, the tissue sections were sealed with a quick-drying neutral resin (ZSZSGBBIO, ZLI-9516).

Tissue Clearing and Staining

The paraformaldehyde-fixed mouse brain tissues were treated with 1/2 CUBIC-L solution (80 mL Milli-Q, 5 g Triton X-100, 5 g N-butyldiethanolamine (Aladdin, 102-79-4)) at 37°C for 6 h. Then, the solution was replaced with a CUBIC-L solution and continued to be treated at 37°C for 15 days, with the new CUBIC-L

solution being replaced every 2 days. The brain tissue was washed three times with staining buffer (1.5 M NaCl). The hyalinised brain groups were transferred to a staining buffer containing vascular and Aβ probes for fluorescence staining (RT, 3 days). The refractive index was adjusted using CUBIC-M solution (25 g Milli-Q, 45 g antipyrine (Aladdin, 60-80-0), 30 g N-methylnicotinamide (Aladdin, 114-33-0), 125 μl of N-butyldiethanolamine). Samples were cleared and stored in dibenzyl ether (Sigma-Aldrich) until light sheet imaging. Images were analysed using Amira and iMaris software. Vascular staining was performed with lectin (Vector, DL-1178-1, 1:100) and Aβ staining was performed with MCAAD (abcam, ab216983, 100 nM). All the buffers were supplemented with 0.2% Proclin (Macklin, C15057814) to prevent bacterial and fungal growth.

High Performance Liquid Chromatography (HPLC)

Donepezil HCl (Aladdin, D129948) dissolved in PBS was added to a polymer film to prepare donepezil HCl@A_{39}-POs, followed by dialysis using a 3 kDa dialysis bag for 7 days. The concentration of donepezil HCl in the dialysis fluid was measured to calculate the encapsulation efficiency. Sodium 1-decanesulfonate (Aladdin, S100284) was dissolved in pure water (15.7416 mM/L) and filtered. Chromatographic grade acetonitrile solution and perchloric acid were added, followed by ultrasonication for 10 min. Standard solutions of

donepezil HCl at concentrations of 250, 125, 62.5, 31.25, 15.625, and 7.8125 μg/ml were prepared. The content of donepezil HCl was detected using an Agilent-1260 chromatograph under the conditions of a flow rate of 1 ml/min, column temperature of 35°C, volume of 20 μl, and detection signal at 271 nm.

Morris Water Maze (MWM) Experiment

In each group, mice were administered a caudal vein injection daily (A_{39}-POs, Donepezil@A_{39}-POs, Donepezil, or saline), continuing for three consecutive days. Following this, mice were housed in a standard rearing environment for seven days to acclimatise and recover. For the analysis, the pool was segmented into four quadrants centred around the circle. From days 11 to 14, a platform was positioned in the first quadrant, and animals were randomly introduced into the thermostatic pool from the midpoint of the outer wall of each quadrant daily, with the time taken by the mice to locate the platform recorded as the escape latency. Should mice fail to reach the platform within 120 s, they were guided to it and remained there for 30 s. A spatial probe was conducted on day 15. With the platform removed, mice were placed into the water from the midpoint of the pool edge in the third quadrant. The results of the spatial probe were expressed as either the percentage of time the mice remained at the original escape platform location or the number of times they passed the original platform location. Reverse Place Navigation trials were

conducted from days 16 to 19, with the platform positioned in the quadrant opposite the original platform location (first quadrant). The animals repeated the training regimen from days 11 to 14, and reverse escape latency was documented. On day 20, the platform was removed, and mice were introduced into the water from the midpoint of the edge of the first quadrant. The results of the Reverse spatial probe were expressed as either the percentage of time that the animal spent on the escape platform or the number of times it crossed the original platform position. The tracking system (Ethovision XT, Noldus Information Technology) recorded the animals' swimming speed, passing length, the number of times crossing the platform, and escape latency.

2. Extended figures

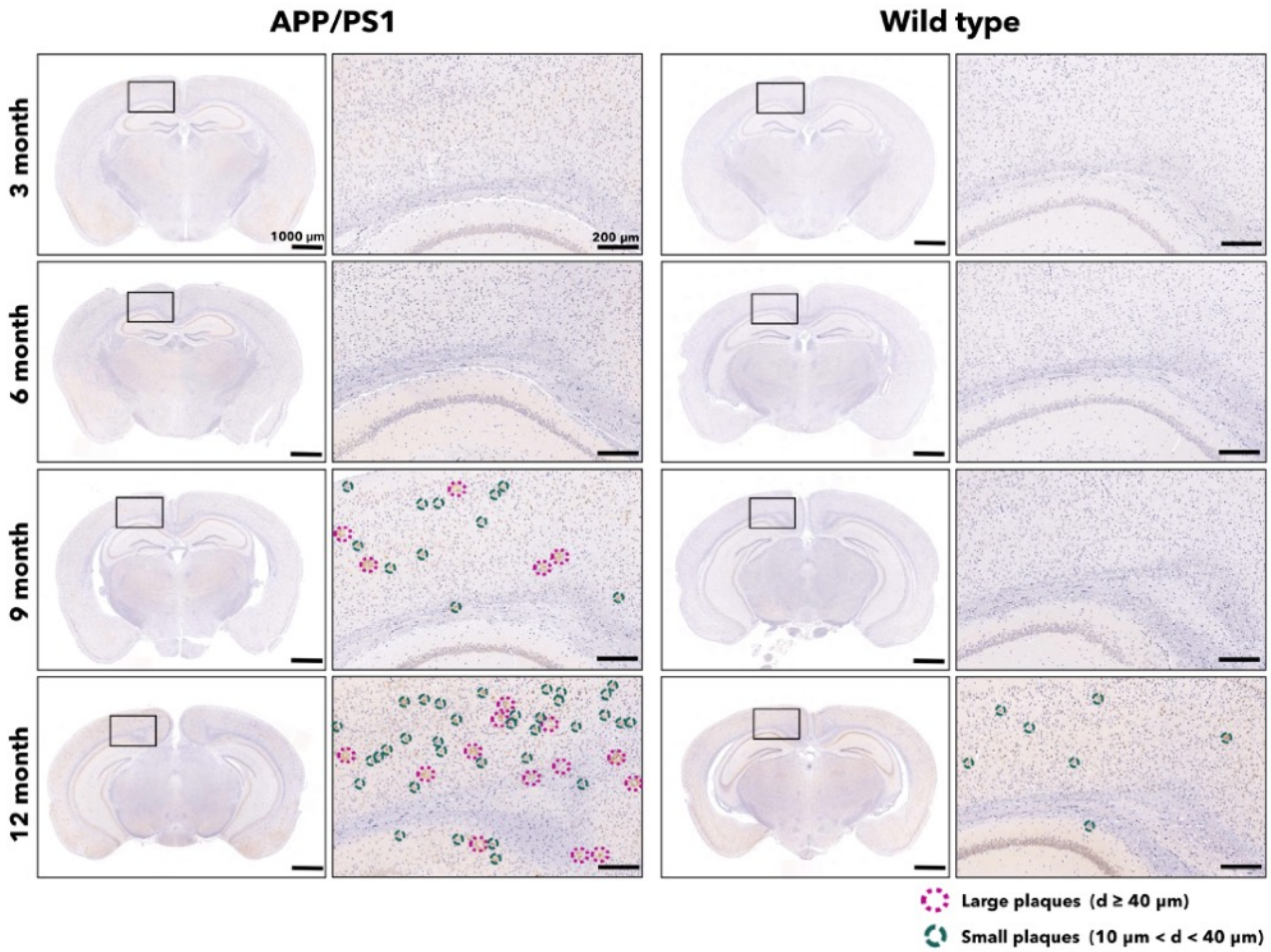

Fig. S1. IHC images of Aβ in the brains sections of age-matched mice (n = 3). IHC images of Aβ in coronal brain sections from mice at 3, 6, 9, and 12 months old. Each section is derived from a different mouse brain. As age increases, area percentage of the brain occupied by Aβ increases in both APP/PS1 and wild type mice.

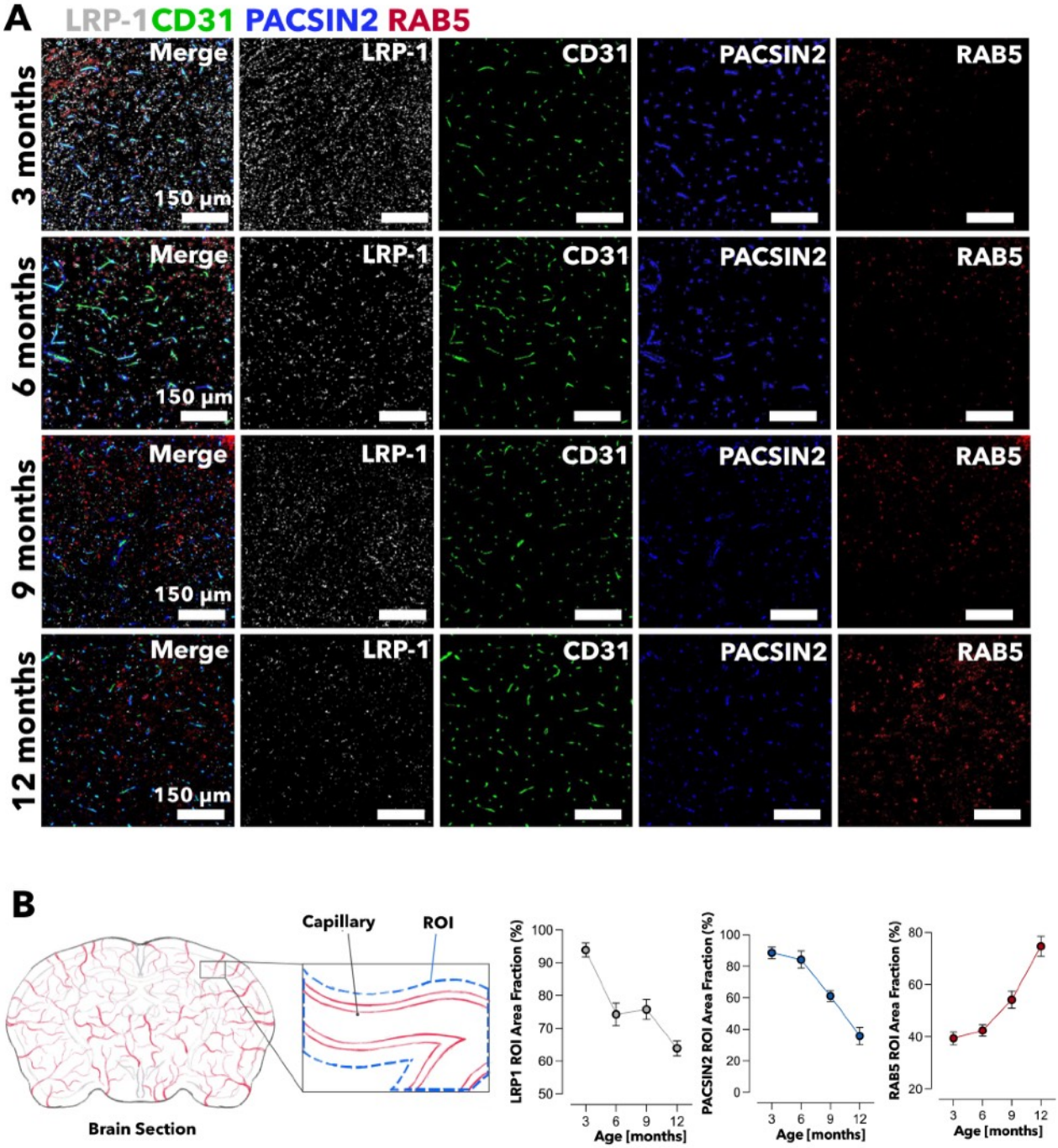

Fig. S2. Fluorescence micrographs colocalisation analysis of age-matched brains. (A) Fluorescence images of brain sections from 3, 6, 9, and 12 months old wild-type mice, LRP1 (grey) CD31 (green) PACSIN2 (blue) RAB5 (red). (B) Capillary regions were counted as ROIs, and the percentage area of LRP1, PACSIN2, and RAB5 in the ROIs was counted. A total of 10 capillaries from two independent trials were selected for counting. LRP1, PACSIN2, and RAB5 followed the same trend as in the ELISA assay.

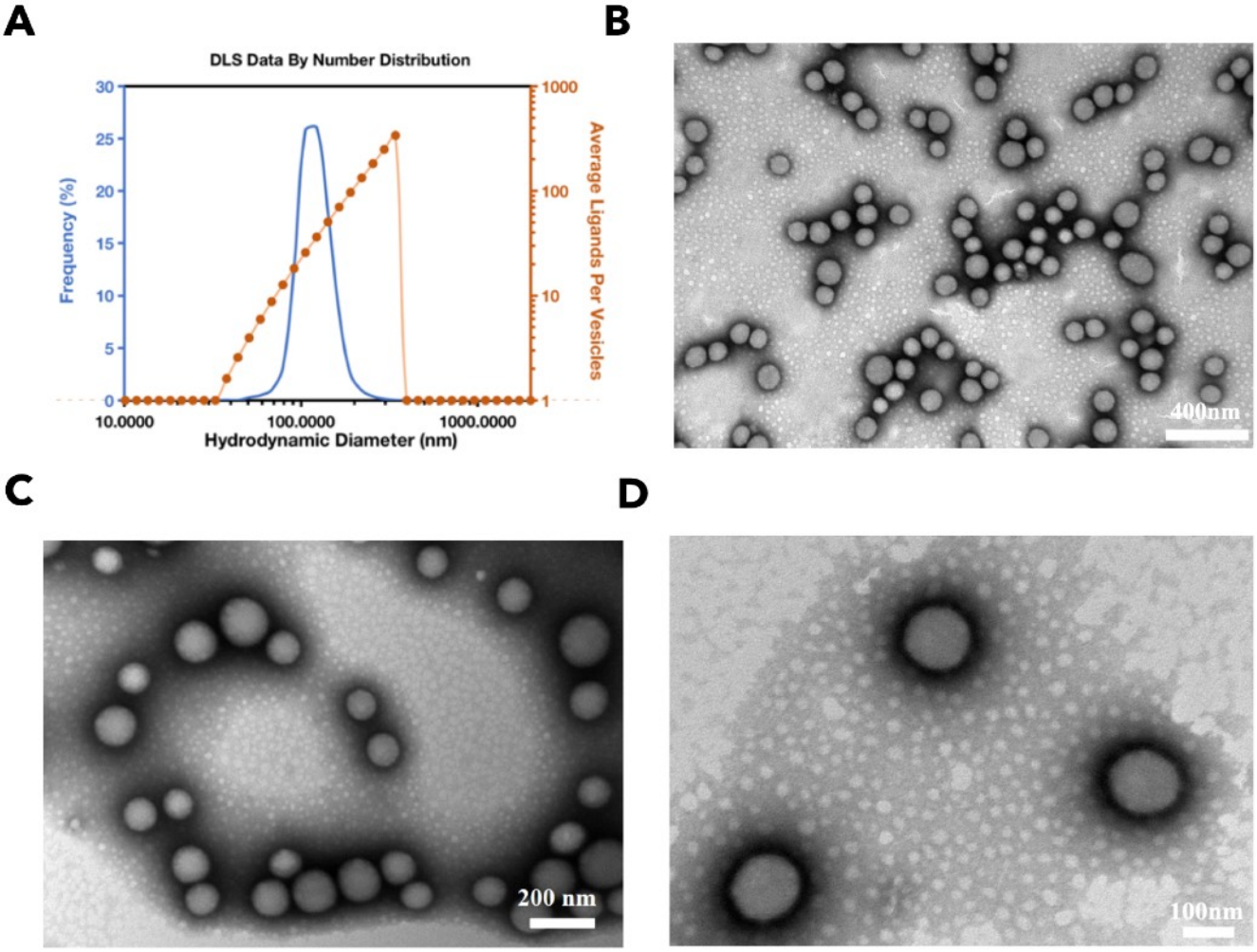

Fig. S3. Characterization of A_{39}-POs in terms of size and morphology. Size distribution and diameter matched ligands number of A_{39}-POs (A). TEM images of A_{39}-POs magnified 60,000 × (B), 100,000 × (C) and 140,000 × (D)

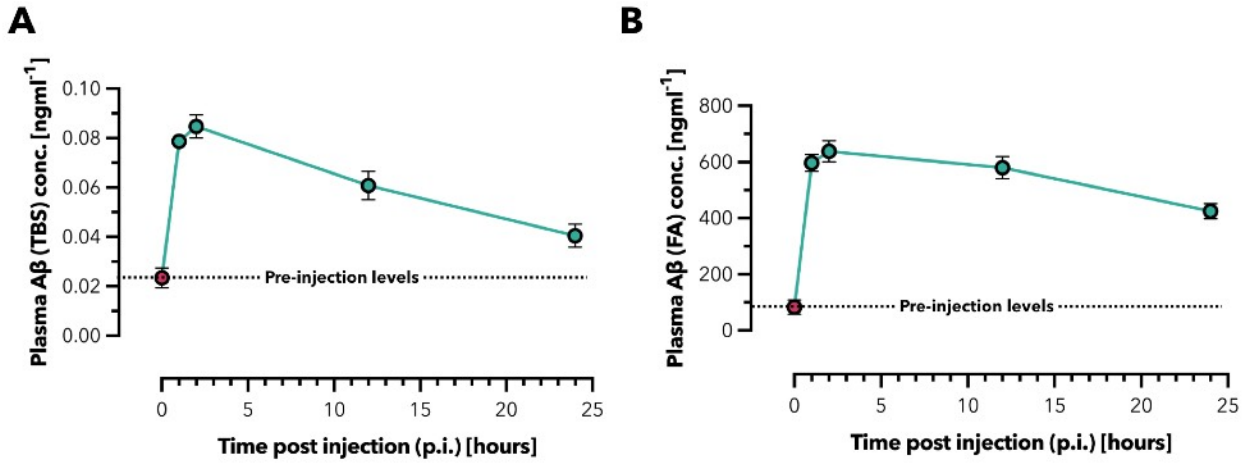

Fig. S4. The administration of A_{39}-POs markedly increased the concentration of blood Aβ within a brief timeframe. (A) Concentrations of Aβ extracted with TBS in plasma at various post A_{39}-POs injection time points. (B) Concentrations of Aβ extracted with formic acid (FA) in plasma at various post A_{39}-POs injection time points. Following the I.V. of A_{39}-POs, the concentration of Aβ in the plasma increased several fold, reaching a peak at two hours post A_{39}-POs injection. Subsequently, the concentration of Aβ gradually decreased.

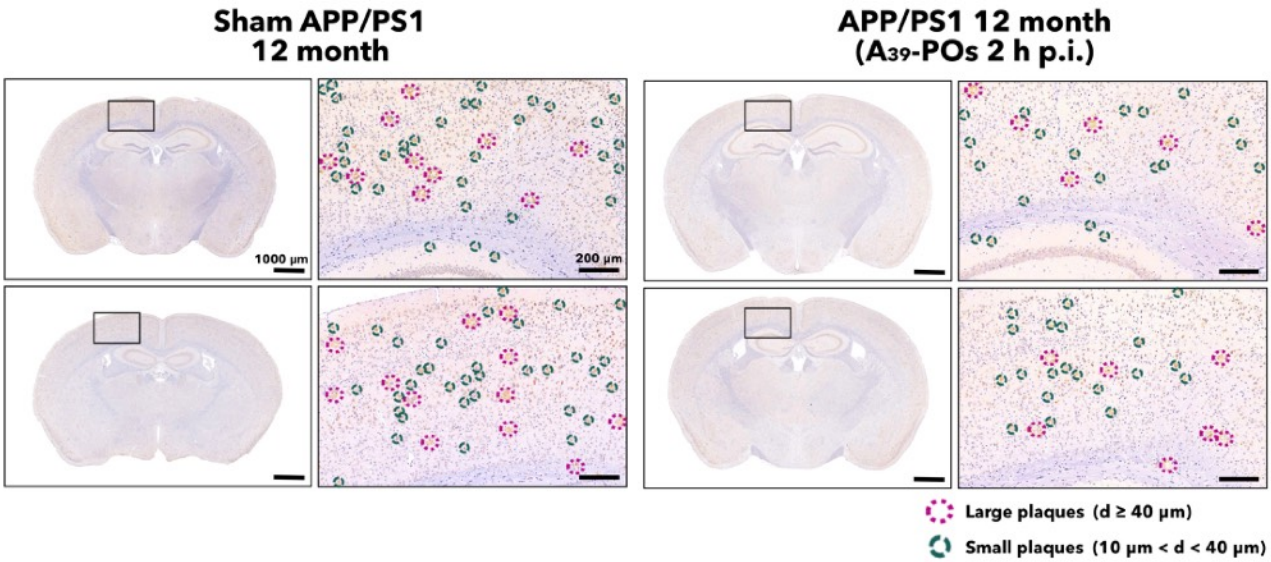

Fig. S5. IHC images of Aβ in the brain sections of 12-month-old Sham APP/PS1 and A_{39}-POs treated mice. IHC images of Aβ in coronal brain sections from 12-month-old mice. Each section is derived from a different mouse brain. The percentage of the brain area occupied by Aβ plaques reduced after 2 h post A_{39}-POs injection. Meanwhile, both the number of large and small plaques decreased.

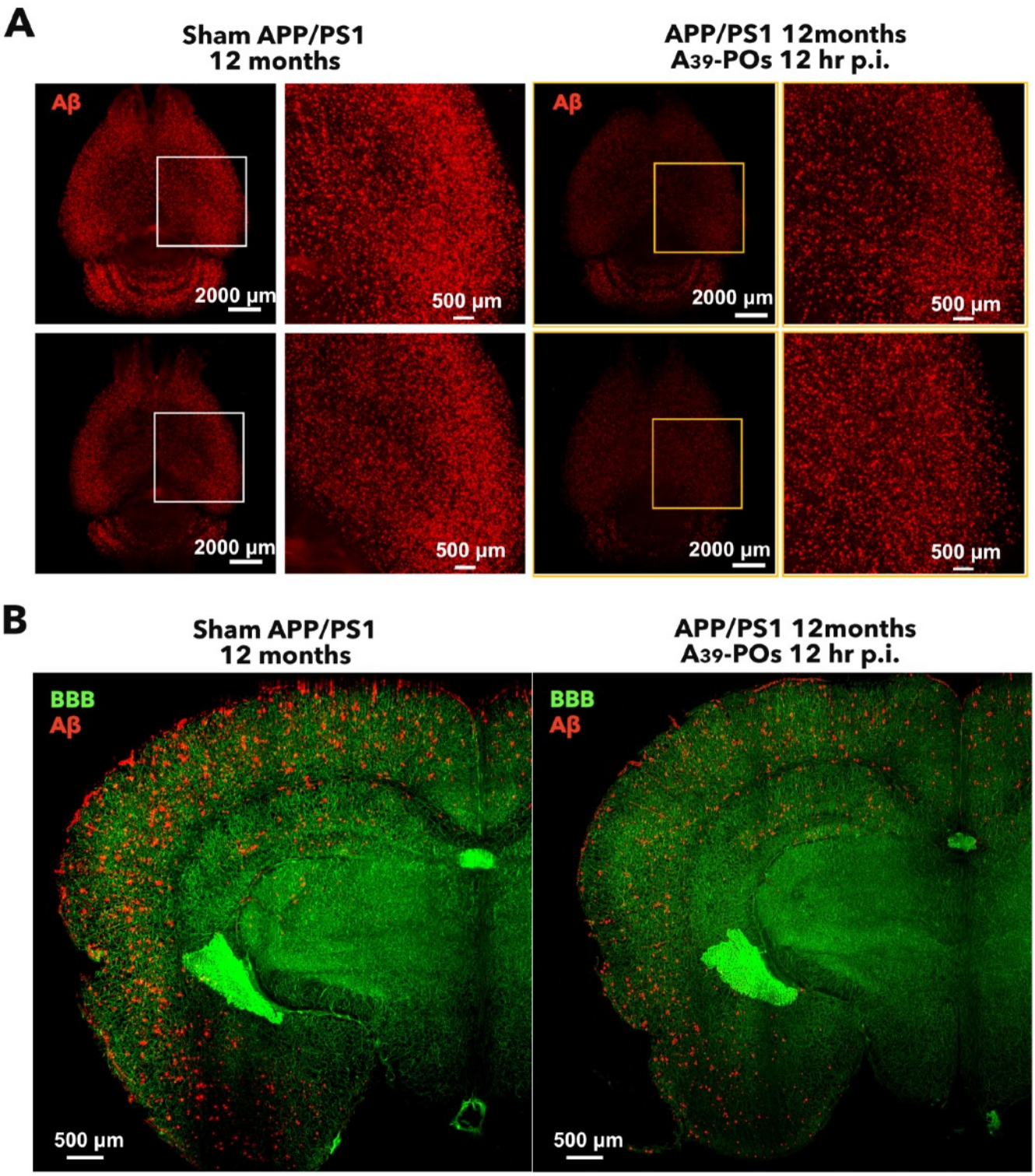

Fig. S6. Brain clearing images of 12-month-old Sham APP/PS1 and A_{39}-POs treated mice. (A) 3D brain clearing images of Aβ (red) in the mice brain. (B) Coronal view of mouse brain with a thickness of 300 μm (BBB in green, Aβ in red). The Aβ signal is attenuated in the brains treated with A_{39}-POs.

Fig. S7. Fluorescence micrographs co-localisation analysis of treated brain. (A) Fluorescence images of brain sections from 12-month-old wild-type AD and treated AD mice, LRP1 (grey) CD31 (green) PACSIN2 (blue) RAB5 (red). (B) Confocal microscope image of brain sections from 12-month-old wild-type AD and treated AD mice. (C) Capillary regions were counted as ROIs, and the percentage area of LRP1, PACSIN2, and RAB5 in the ROIs was counted. A total of 10 capillaries from two independent trials were selected for counting. LRP1, PACSIN2, and RAB5 followed the same trend as in the ELISA assay.

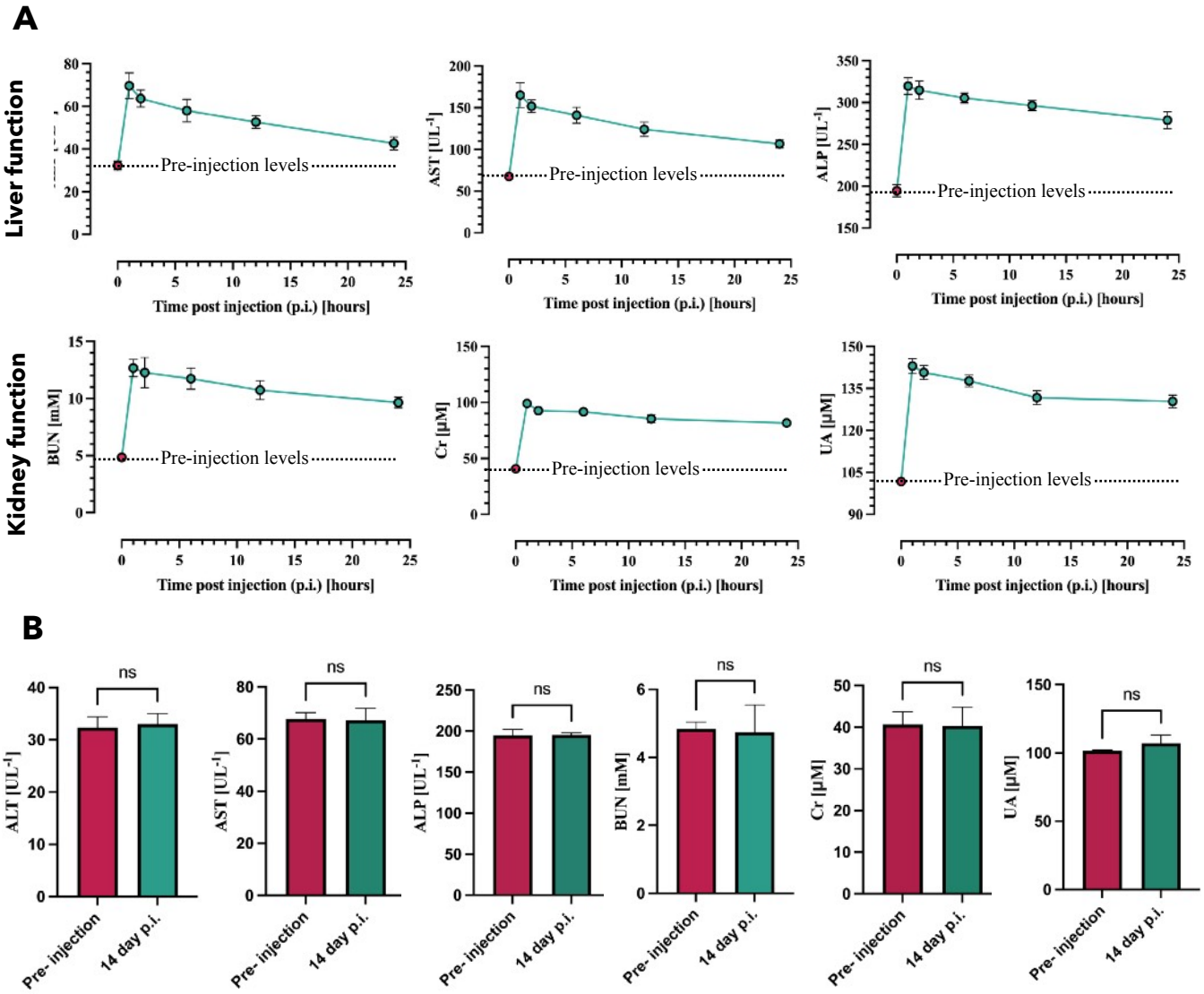

Fig. S8. Blood biochemical tests to evaluate the biosafety of A_{39}-POs. Liver (ALT, AST and ALP) and Kidney (BUN, Cr and UA) function test of A_{39}-POs. (A) Time post injection of 1 h, 2 h, 6 h, 12 h and 24 h. (B) Time post injection of 14 days. After 14 days, liver and kidney index back to pre injection level.

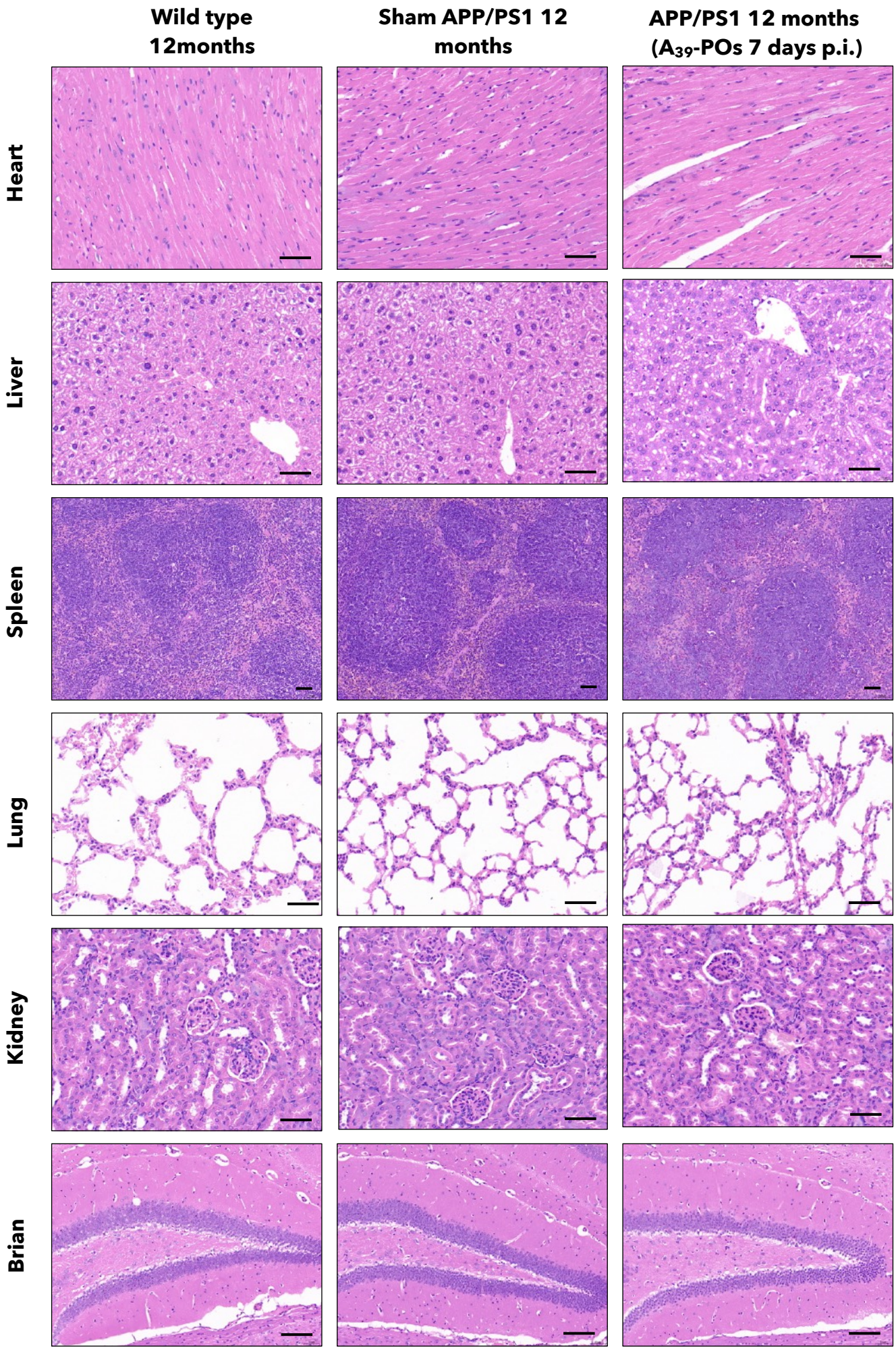
Wild type 12months
Sham APP/PS1 12 months
APP/PS1 12 months (A_{39}-POs 7 days p.i.)
Heart
Liver
Spleen
Lung
Kidney
Brian

Fig. S9. H&E staining to evaluate the biosafety of A_{39}-POs. Heart, liver, spleen, lung, kidney, and brain H&E staining of WT, AD, and A_{39}-POs treated mice. The cells of A_{39}-POs treated mice's tissues and organs did not show nuclear crumpling and cellular deformation. All Scale bars = 50 μm, animals with the age of 12 months.

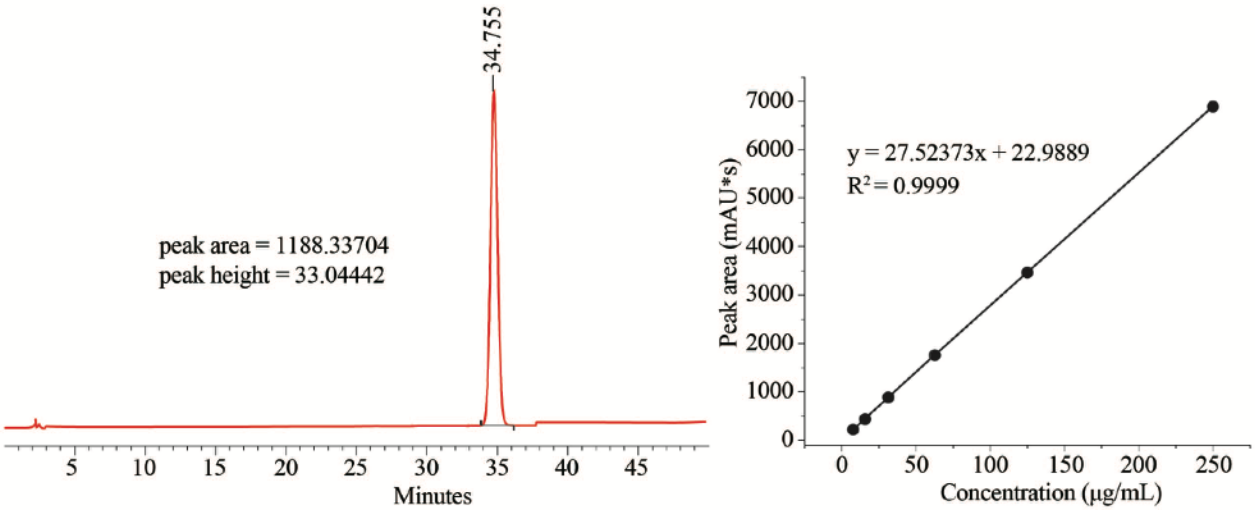

Fig. S10. HPLC methodology was employed to ascertain the encapsulation efficiency following the encapsulation of Donepezil within A_{39}-POs. The peak area and peak height of the Donepezil@POs dialysate are depicted on the left. The corresponding standard curve is presented on the right. (Encapsulation efficiency = 20.68%)

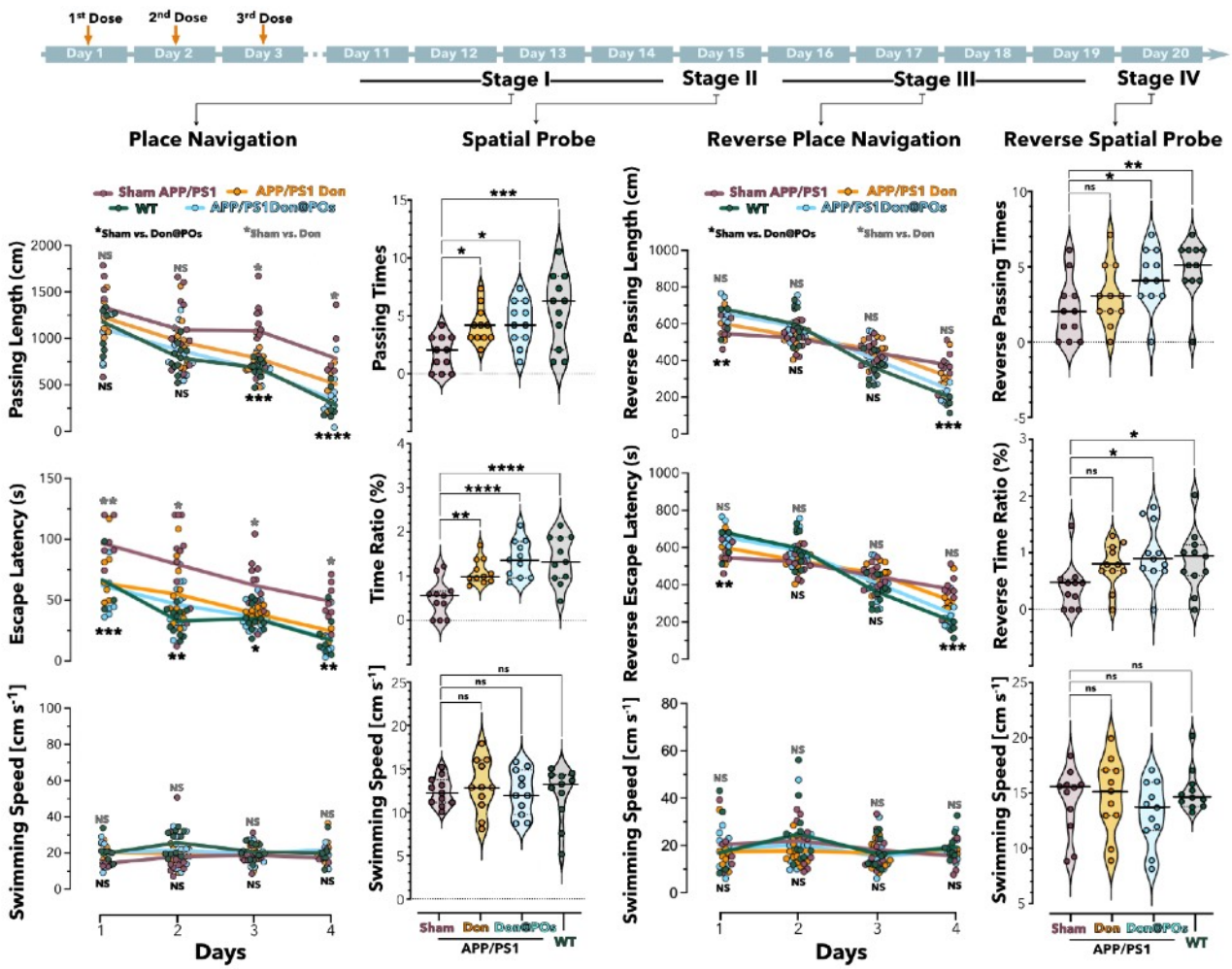

Fig. S11. Donepezil@POs can treat AD and produce similar therapeutic effects to A_{39}-POs, which are superior to the same dosage of free donepezil. Mice were injected with saline (Sham APP/PS1 group, WT group), Donepezil@POs (Don@POs group, 10g/L 200μL) or Donepezil (Don group, 2g/lL 200μL) once a day for the first three mornings. Recovery was observed from days 4 to 10 under original rearing conditions. (Stage I) Place navigation test occurred on days 11-14, showing a gradual decrease in passing length and escape latency for finding the escape platform across all groups, with the APP/PS1 Don@POs group matching the WT level and significantly outperforming the Sham APP/PS1 group. Meanwhile, the Don group demonstrated space exploration capabilities superior to Sham APP/PS1. But not to the level of the Don@POs. (Stage II) On day 15, during the (spatial probe), APP/PS1 Don, APP/PS1 Don@POs, and WT groups demonstrated more passing times and a higher

percentage of time spent at the escape platform's original location. (Stage III) The reverse place navigation trial from days 16-19, with the platform moved to the opposite side, the APP/PS1 Don@POs and WT groups initially took longer, indicating stronger spatial memory from the stage I and stage II. However, their reverse passing length and escape latency decreased rapidly over time and were significantly lower than those of the Sham APP/PS1 mice. In this stage, which is more difficult compared to stage I and II, the Don group never showed a statistically significant difference in levels from the Sham APP/PS1 group. (Stage IV) On day 20, in the reverse spatial probe test without the platform, Don@POs treated mice still outperformed the Sham APP/PS1 group. The Don group outperformed the Sham APP/PS1 group as well, but not to the level of the WT group. Place navigation trials (Phases I and III) were analysed using two-way ANOVA, while spatial probe trials (Phases II and IV) comparisons used one-way ANOVA. Significance levels are denoted as *$p<0.05$, **$p<0.01$, ***$p<0.001$, ****$p<0.0001$, with $n = 11$.

References

1. X. Tian, S. Nyberg, P. S. Sharp, J. Madsen, N. Daneshpour, S. P. Armes, J. Berwick, M. Azzouz, P. Shaw, N. J. Abbott, G. Battaglia, LRP-1-mediated intracellular antibody delivery to the central nervous system. Sci. Rep. 5, 11990 (2015).